Effects of various parameters on numerical simulations of inertial confinement fusion hohlraum and radiation hydrodynamics

N.K. GUPTA AND B.K. GODWAL

High Pressure Physics Division, Bhabha Atomic Research Centre, Trombay, Mumbai—400 085, India

(RECEIVED 5 June 2000; ACCEPTED 9 December 2000)

Abstract

In this article, we study the effect of various parameters on the estimation of radiation temperature inside an indirect drive ICF hohlraum and also study the hydrodynamics of aluminum and gold foils driven by the hohlraum radiation. A multigroup one-dimensional, radiation hydrodynamic code is used for this study. Opacities are calculated using a screened hydrogenic average atom model. We also investigate the opacities of Au-Sm and Au-Gd mixtures. It is shown that the mixing of two high Z materials can lead to an enhancement in the Rosseland means, which is of direct interest in indirect-drive inertial confinement fusion. The radiation temperature inside a cylindrical hohlraum is seen to be strongly dependent on the number of frequency groups used. One group radiation transport underpredicts the radiation temperature. It is shown that erroneous results can be obtained if the space mesh in the hohlraum wall is not fine enough. The spectrum of the radiation inside the hohlraum is seen to be different from Planck, especially in the high-energy range. This may lead to preheating of the target. Hydrodynamics of an aluminum foil driven by the hohlraum radiation is also presented in this article. A scaling law for the radiation-driven shock-wave speed in the gold foil is obtained.

Keywords: Hohlraum; Hydrodynamics; ICF; Mixture opacities; Radiation transport

1. INTRODUCTION

Most of the present day inertial confinement fusion (ICF) experiments are based on the concept of indirect drive (Lindl, 1998). Although some of the recent smoothening devices like random phase plate (RPP), smoothening by spectral dispersion (SSD), induced spatial incoherence (ISI), and so forth (Nishihara *et al.*, 1994) have kept interest alive in direct-drive targets, indirect-drive fusion schemes have a distinctive advantage because of uniform radiation inside. The uniformity of the radiation inside the hohlraum is of great significance for the success of ICF experiments. For example, it is shown by Ermolovich *et al.* (1998) that a nonuniformity of 5% in the radiation temperature on the pellet surface can reduce the neutron yield by a factor of seven. The current high-pressure experiments are essentially using the hohlraum as a source of soft X rays to drive the shock wave in the material. To minimize the energy loss in converting the laser or ion beam to X rays, high reemis-

sion from hohlraum walls and higher X-ray conversion efficiency is required. This requires the use of high-*Z* material and gold has been the most widely used material so far for the ICF hohlraum fabrication. Recently, it has been proposed to use a mixture of two high-*Z* elements (Nishimura *et al.*, 1993; Orzechowski *et al.*, 1996; Wang *et al.*, 1997; Colombant *et al.*, 1998). These studies have shown that it is possible to obtain higher Rosseland mean opacity as compared to either of the two elements in the mixtures. This in turn can lead to higher conversion efficiency of laser light and reemission from the hohlraum wall and hence higher radiation temperatures. To numerically simulate an indirect-drive ICF experiment, the two basic requirements are the radiation hydrodynamics and the computations of the frequency-dependent radiation opacities. Any model to calculate opacities must include bound–bound transitions, as their absence can change the results by a factor of two (Mayer, 1947). In this article, we very briefly describe the models of opacity and radiation hydrodynamics used. In Section 2, we briefly describe the model used for computing the opacities and its validation. We also present in this section our results on the enhancement of Rosseland mean due to mixing of two high-*Z* elements. Section 3 contains the

---

Address correspondence and reprint requests to: N.K. Gupta, High Pressure Physics Division, Bhabha Atomic Research Centre, Trombay, Mumbai—400 085, India. E-mail: nkgupta@apsara.barc.ernet.in

description of the radiation hydrodynamics model and numerical simulation results for a cylindrical hohlraum. Although two-dimensional codes like LASNEX (Zimmerman & Kruer, 1975) are widely used for such simulations, the aim of the present studies is to look into the effects of number of frequency groups and the wall mesh spacing on radiation temperature inside the hohlraum. For this, we used a simple and fast one-dimensional code to bring out the sensitivities of these parameters on the estimation of radiation temperature inside the hohlraum. We also present in this section the main results of simulation of a radiation-driven shock wave in a wedge-shaped aluminum foil. A scaling law is obtained for the radiation-driven shock-wave speed in gold foil. Finally, we conclude the paper in Section 4.

2. MODEL FOR THE OPACITY CALCULATIONS

Following the work of Rickert and Meyer-ter-vehn (1990), we used the screened hydrogenic atom model of More (1982) including the l-splitting as proposed by Perrot (1989). The energy spectrum of partially ionized ions is calculated using the screened hydrogenic model including the l-splitting. The 10-by-10 matrix of the screening constants used is the one proposed by More (1982). The l-splitting introduces an additional 10 constants as given by Perrot (1989). For the broadening of each line, standard formulas are used for Lorentz and Doppler broadening. The fine structure and stark broadening are calculated in hydrogenic approximation. The oscillator strength for a transition from bound state (n, l) occupied by P_{nl} electron to a bound state with occupation number $P_{n'l'}$ is evaluated as

$$f_{nl,n'l'} = \frac{1}{3} \frac{\text{Max}(l, l')}{2l + 1} \frac{\Delta E}{13.6 \times 10^{-3}} (R_{nl,n'l'})^2 P_{nl} \left(1 - \frac{P_{n'l'}}{2(2l' + 1)}\right).$$

(1)

For a bound-free transition, the oscillator strengths are written as

$$\frac{df_{nl}}{dh\nu} = 4.927 \times 10^{-3} h\nu (h\nu - I_{nl})^{1/2}$$

$$\times P_{nl} Q_\epsilon \left[\frac{l + 1}{2l + 1} (R_{nk, \epsilon l+1})^2 - \frac{1}{2l + 1} (R_{nl, \epsilon l-1})^2 \right],$$

$$h\nu \geq I_{nl}, \qquad (2)$$

where $h\nu$ and I_{nl} are, respectively, the photon and ionization energies in kiloelectronvolts. ΔE denotes the energy difference between the level (n, l) and (n', l'). ϵ denotes the kinetic energy of the unbound state. The radial integrals $R_{nl,n'l'}$ and $R_{nl,\epsilon l\pm 1}$ are evaluated using hydrogenic wave function with appropriate effective charges (Naqvi,

1964). We use Fermi–Dirac statistics to evaluate the availability factor Q as

$$Q_\epsilon = 1 - \frac{1}{1 + \exp(\alpha + \epsilon/T)}. \qquad (3)$$

The chemical potential α is obtained by solving the equation

$$F_{1/2}(\alpha) = 2.795 \times 10^{-3} \frac{Z_0 \rho}{A T^{3/2}}, \qquad (4)$$

where $F_{1/2}(\alpha)$ is the Fermi–Dirac integral of order $\frac{1}{2}$. A is the atomic number and the average degree of ionization Z_0 is obtained as

$$Z_0 = Z - \Sigma_{nl} P_{nl}. \qquad (5)$$

ρ and T denote the plasma density and temperature, respectively. The occupation numbers P_{nl} are evaluated in an iterative manner taking into account the effect of pressure ionization. The other details about the model are as described by Rickert and Meyer-ter-vehn (1990) and are therefore not repeated here. We use a nonuniform frequency mesh with increasing mesh width as we move toward the higher photon energies (Gupta, 1999). A total of 5000 frequency points are used for all the results presented in this article. As a representative of mean opacities, we show in Figure 1 the Rosseland and Planck mean opacities as a function of temperature for aluminum at a density of 2.15×10^{-3} g/cc. A wide variation of temperatures from 1 eV to 100 KeV is presented in this figure. At higher temperatures, Planck mean approaches zero as no scattering is included in it. The Rosseland mean approaches a constant Thomson scattering value as bound–bound, bound–free, and free–free contribution approaches zero at high temperatures. Also shown in this figure is the maximum Rosseland mean K_{Max} as per the maximum opacity theorem (Armstrong & Nicholls, 1972)
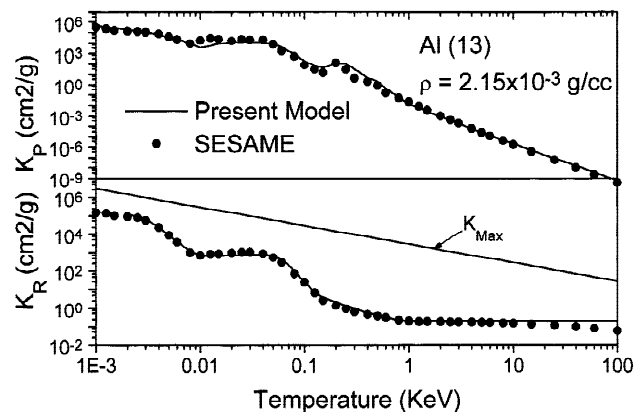

Fig. 1. Rosseland and Planck mean opacities as a function of temperature for aluminum at density $\rho = 2.15 \times 10^{-3}$ g/cc. The curve marked K_{Max} denotes the Rosseland mean as per the maximum opacity theorem.

and the SESAME table (T-4 group, 1983) data. The calculated mean opacities are seen to be in excellent agreement with the SESAME data. Also, the K_{Max} is seen to be consistently higher than the Rosseland mean throughout, as is expected.

2.1. Opacities of mixtures

For the case of mixtures, the bound–bound and bound–free contribution to opacities are obtained as weighted averages. The weights for each element in the mixture are taken as the respective number fraction. Free–free contribution to opacities of mixture is obtained using weighted average ionization of the mixture. The average degree of ionization of the mixture is obtained from the individual element ionization with their fraction density as the weights (Rose, 1992).

Nishimura *et al.* (1993) proposed the use of Au-Sm and Au-Tb mixtures and they showed the conversion efficiency of the mixtures containing ~20% gold to be higher than those of the pure materials. Wang *et al.* (1997) used an unresolved transition array (UTA) model of opacity calculations and showed the Rosseland mean opacities of Au-Sm and Au-Gd mixtures to be notably higher than that of pure Au. Orzechowski *et al.* (1996) used a sophisticated code XSN, where bound–bound transitions play a central role, to show that opacity of a 50–50 mixture of Au-Gd can improve by a factor of 1.7 to that of pure Au. They also showed that a 50% increase in the hohlraum wall opacity results in a 12% less energy requirement for the same hohlraum temperature. Colombant *et al.* (1998) studied a variety of mixtures and showed that almost any mixture of gold with another material will have higher Rosseland mean opacity as compared to the pure gold. They also studied the mixtures of more than two elements to optimize the enhancement in the opacity of the mixture.

We may mention here that although all the above mentioned models predict an enhancement in the Rosseland mean opacity of the mixtures, the exact increase in value differs from model to model. For example, Nishimura *et al.* (1993) show a much higher increase in the opacity of mixtures as compared to Wang *et al.* (1997). We study the opacities of Au-Sm and Au-Gd mixtures using the average atom model described previously. We note that the Planck mean of any mixture will always lie between the Planck means of the elements in the mixture. It is only the Rosseland mean which can be higher than the Rosseland means of both the elements in the mixture. This happens when the peaks in the opacity versus frequency curve of one element coincide with the valleys of the other element. Clearly, these are the bound–bound and bound–free transitions which play the crucial role in enhancing the Rosseland mean of the mixtures. In Figure 2, we show the bound–bound contribution of opacities for Au and Sm at a density of 0.01 g/cc and a temperature of 350 eV. The solid line represents the gold results while the dotted line represents the corresponding values of Sm. From this figure we note the desired features
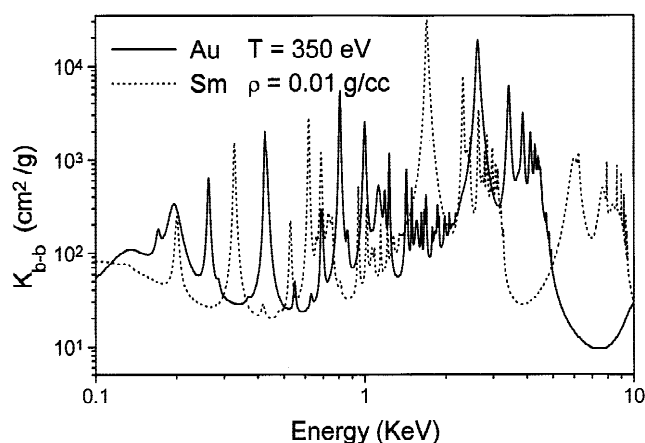

Fig. 2. Bound–bound contribution to opacities for Au and Sm at a temperature of 350 eV and density of 0.01 g/cc.

of valley and peak combinations. For example, Sm opacities clearly show peaks at about 300 eV, 1.08 KeV, and 1.8 KeV, while the Au curve shows valleys here. One can identify such features at a number of other places from this figure and thus we expect a mixture of Au and Sm should lead to higher Rosseland mean opacities. Figure 3 shows the bound–free contribution to opacities for these two elements. For energies greater than 1 KeV, we again observe the desired features in the opacity curves. The steplike shape of the curve in this figure corresponds to the opening up of various energy levels. In Figure 4, we show the variation of Rosseland mean with temperature for gold (dashed line), Samarium (dotted line), and a 50–50 mixture of Au-Sm (solid line) for the density of 0.01 g/cc. From this figure we note that opacity of Au-Sm mixtures is more than Au or Sm separately at all the temperatures. In Figure 5 we show the Rosseland mean for the mixture as a function of gold fraction. The plasma density is 0.1 g/cc and temperature is
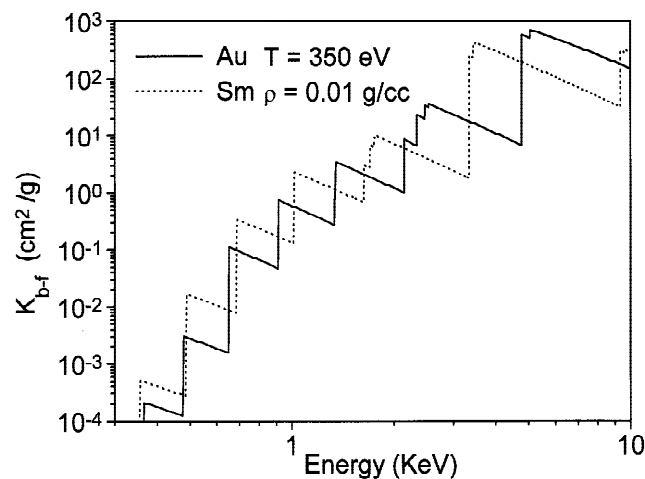

Fig. 3. Bound–free contribution to opacity for Au and Sm at a temperature of 350 eV and density of 0.01 g/cc.
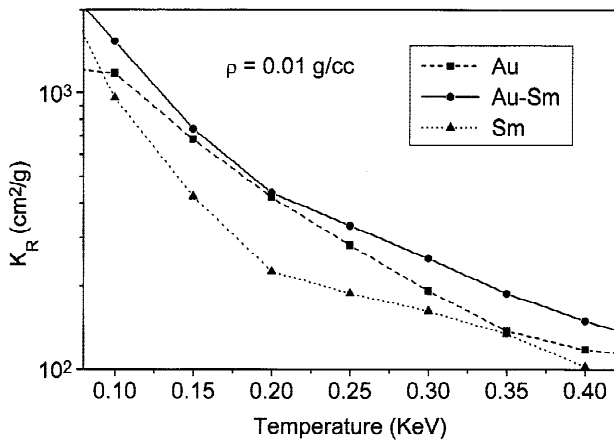
Fig. 4. Rosseland mean opacity for Au, Sm, and a 50–50 mixture of Au and Sm as a function of temperature for the plasma density of 0.01 g/cc.

Fig. 6. Rosseland mean opacity of gold, gadolinium, and a 50–50 mixture of gold and gadolinium as a function of plasma temperature. The plasma density is 0.1 g/cc.

200 eV. The mean is normalized to the pure gold value. Square marker points in this figure are the values taken from the article of Wang *et al.* (1997). Our results slightly over-predict the Rosseland mean of the mixture as compared to Wang *et al.* (1997). However, at higher temperatures, the trend changes and our model underpredicts the mixture means. We have also studied the mixture of gold and gadolinium. In Figure 6, we show the plot of enhancement factor for Au-Gd mixture as a function of the Au fraction. The enhancement factor is defined as the ratio of the Rosseland mean of the mixture to that of pure gold. This factor is thus a measure of benefit for mixing any element in the gold. We note that for a low temperature (100 eV), an enhancement in Rosseland mean up to 55% is possible over gold. Also note that at 100 eV, the Rosseland mean of gadolinium is more than that of gold, while for higher temperatures, the latter one increases. Thus we observe that the Rosseland mean
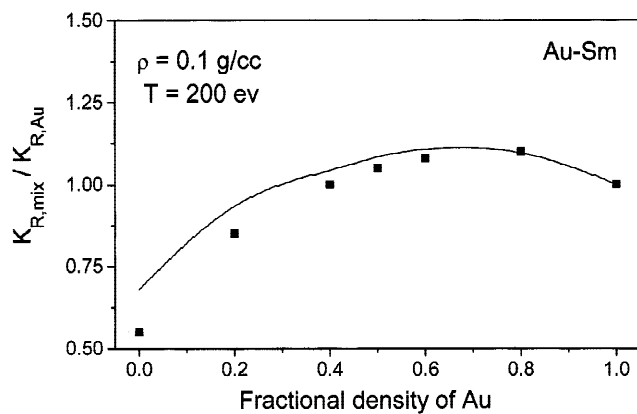
opacities of Au-Sm and Au-Gd mixtures are more than that of the individual materials in the mixture. We have restricted our attention to only two mixtures, namely Au-Sm and Au-Gd. There are certainly many more such mixtures (Colombant *et al.*, 1998).

3. MODEL FOR THE RADIATION HYDRODYNAMICS

The hydrodynamics of the ICF target is treated by solving the standard three conservation (mass, momentum, and internal energy) equations in one-dimensional Lagrangian geometry (Zel'dovich & Raizer, 1966). The shocks are treated by the Von-Neumann artificial viscous pressure procedure (Richtmyer & Morton, 1967). The material pressure is related to the density and internal energy through a tabulated equation of state (EOS). For a given density and internal energy, the material temperature is again obtained from tabulated EOS. The laser energy deposition is calculated via inverse bremsstrahlung up to the critical density and a pre-specified fraction of the remaining power is dumped at the critical density point. Most of the thermal flux is carried by the electrons and is calculated using the flux limited Spitzer's formula. Radiation transport is treated by multigroup diffusion approximation (Ramis *et al.*, 1988) or by discrete direction S_n method (Gupta & Kumar, 1995). Tabulated opacity data are used. The other details of the model are similar to the code MULTI developed by Ramis *et al.* (1988) and are therefore not described here.

3.1. Numerical simulation of cylindrical hohlraum

In the experiments conducted at the Lawrence Livermore National Laboratory (LLNL, NOVA facility), 3-mm-long and 1.6-mm-diameter cylindrical gold hohlraum was driven

Fig. 5. Rosseland mean opacity for the Au and Sm mixture as a function of gold fraction. The square points are the values taken from Wang *et al.* (1997).
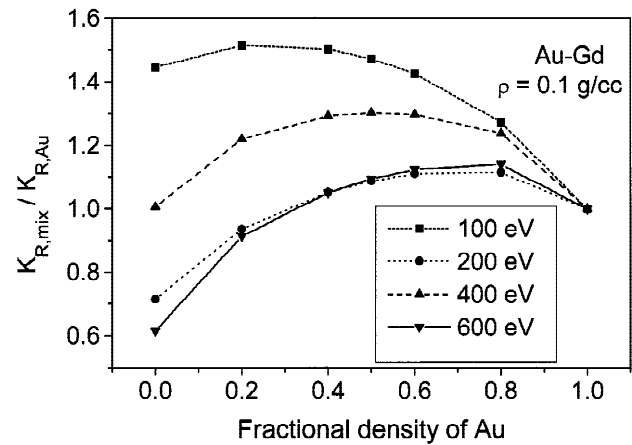
by eight laser beams (Remington *et al.*, 1995). The temporally shaped 3.3-ns laser beams of wavelength 0.351 μm having energies from 2.0 to 3.0 KJ delivered a total peak power of 16 TW/cm^2. We have simulated this experiment using the model described in Sections 2 and 3. Rosseland and Planck means were generated in 1, 100, and 150 groups for a wide variation of density and temperatures. The multigroup boundaries are chosen to be equally spaced in lethargy variable. This leads to a higher number of groups for lower energies. Twenty-one temperature points are used to cover up to 5 KeV, while nine density points cover a range from $1.0 \times 10^{-6}\rho_0$ to $100\rho_0$ (ρ_0 being the solid density). SESAME equation of state (Bennet *et al.*, 1978; Kerley, 1981) is used for these studies. In Figure 7, we show the time-dependent radiation temperature as calculated by the present model using 1, 100, and 150 groups' radiation transport. These results are for a total laser energy of 16.5 KJ incident on the inner surface of the cylindrical hohlraum. The temporal shape of the incident laser beam is as given by Remington *et al.* (1995). The radiation temperature inside the cylindrical hohlraum is seen to be strongly dependent on the number of frequency groups used. Comparing these results with the 2-D calculations of LLNL (Remington *et al.*, 1995), we note that the one group treatment underpredicts the radiation temperature. Foot as well as peak temperatures agree well with the LLNL simulations for 150 groups case. In Figure 8, we show the effect of mesh spacing in the hohlraum wall. In this figure, the curve marked $\nu = 1.0$ refers to uniform mesh grid with a total of 100 meshes. For the other two curves, we used a nonuniform grid with the mesh spacing increasing in a geometric series with the ratio ν as we go from inside to outside. This leads to fine meshes in the crucial region facing the laser beams. From this figure we note that a coarse mesh can lead to a very strong underestimation of remission from the walls. For the case 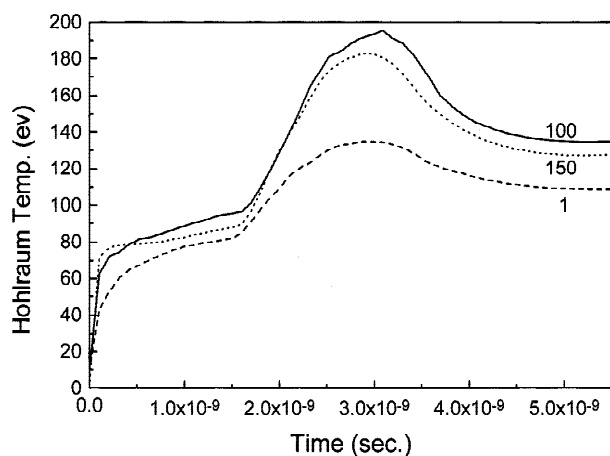of uniform mesh grid, the main peak in the radiation temperature is not seen at all. This is because of low remission from the large size innermost mesh in the hohlraum wall. In Figure 9, we show the spectrum of the radiation inside the hohlraum. The curve marked "foot" in this figure represents the radiation spectrum at 1 ns and it corresponds to the plateau at about 90 eV in Figure 7. The other curve represents the peak spectrum at 3 ns. We do observe the peaks in both these curves at about 2.5 KeV. This non-Planckanian nature of the spectrum can preheat the target unless care is taken in the target design to absorb them.

Fig. 8. The effect of mesh spacing on the radiation temperature inside the hohlraum. The parameter ν is as defined in the text.

3.2. Aluminum foil drive by hohlraum radiation

In this section we consider the experiment of Kauffman *et al.* (1994). A wedge-shaped aluminum foil was driven by a hohlraum radiation and they reported a radiation-driven shock speed of 4.88 cm/μs. The temperature of the radia-

Fig. 7. Calculated radiation temperature inside the hohlraum. Various curves represent the number of frequency groups used in the radiation transport.
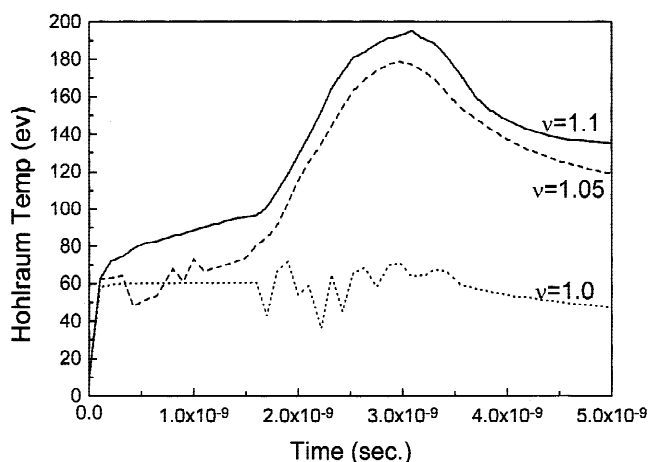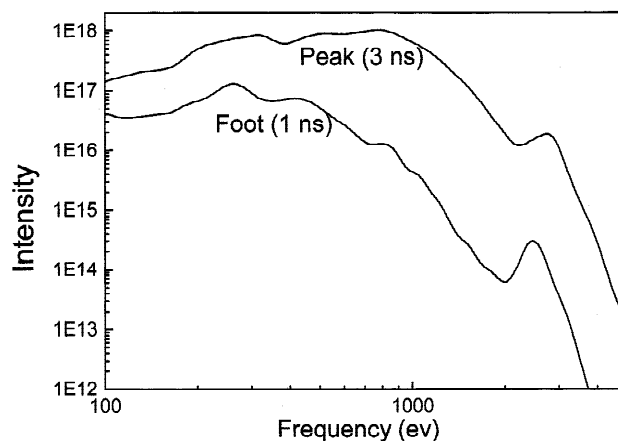

Fig. 9. The calculated frequency dependent spectrum of the radiation inside the hohlraum.
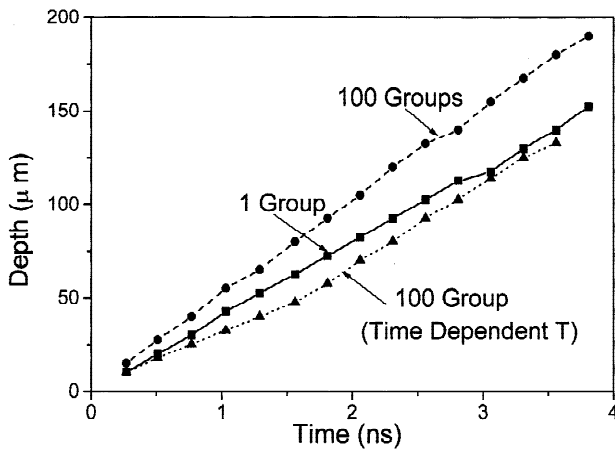
Fig. 10. Radiation-driven shock-wave penetration depth versus time for an aluminum foil. Solid and dashed curves correspond to a time-constant incident flux while the dotted curve represents the results for a time-varying incident temperature as described in the text.

Fig. 11. Radiation-driven shock-wave penetration depth in gold foil for various incident temperatures.

tion in the cavity was estimated in two different ways. Using the scaling laws of shock speed versus radiation temperature for Al, they estimated a radiation temperature of 207 eV. On the other hand, reemission from the X-ray-heated wall is used to estimate time-dependent radiation brightness temperature. It gives an initial temperature of about 135 eV and reaches a peak of 200 eV in about 2.1 ns. Results of our numerical simulation of this radiation-driven hydrodynamics in aluminum foil are shown in Figure 10. The dashed line in this figure represents the penetration of the shock front in the slab for 100 groups of radiation. This gives a shock speed of 4.93 cm/μs as compared to the experimental value of 4.88 cm/μs, showing a good agreement. The solid line represents results for the case of one group simulation. It gives a shock speed of 4.01 cm/μs. For both these cases, the foil was driven by a time-constant incident flux of 207 eV. For the case of a time-varying incident flux, as given in Figure 4 of Kauffman *et al.* (1994), the results are shown in this figure with a dotted curve. From this dotted curve we note that there is a change of slope at about a time of 1.6 ns. The initial slope gives a shock speed of 2.55 cm/μs while the second one gives a speed of 4.75 cm/μs. The first slope corresponds to a plateau of 135 eV while the second slope represents the second plateau at about 200 eV in the incident radiation plot. Scaling laws for shock speed are based on the assumption of time-independent constant incident flux and are therefore not valid in this case. However, if we use the scaling law for aluminum, it gives speeds of 2.49 and 4.61 cm/μs for incident radiation temperatures of 135 and 199 eV, respectively.

We also simulated the radiation-driven shocks in a gold foil. In Figure 11 we show the penetration depth of shock as a function of time for the radiation flux corresponding to black body incident temperatures of 200 eV, 500 eV, 1.0 KeV, and 1.5 KeV. The shock speeds for these temperatures are, respectively, 0.713 cm/μs, 2.28 cm/μs, 4.41 cm/μs, and
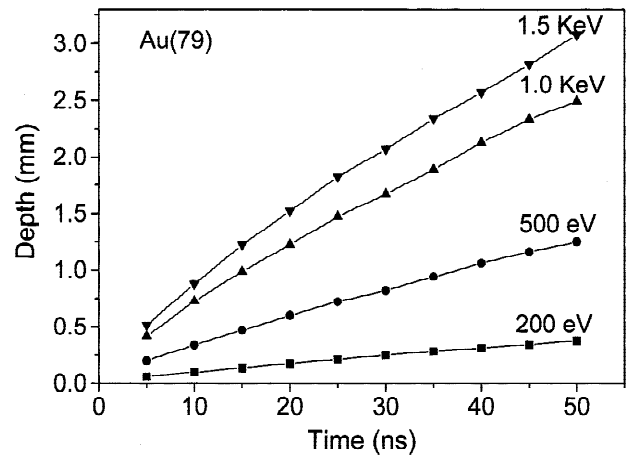
5.5 cm/μs. A best fit of the shock speed to the radiation temperature gives a scaling law

$$U_s \,(\text{cm/s}) = 3.301 \times 10^3 \, T \,(\text{eV})^{1.031},$$

where T denotes the incident blackbody temperature.

4. CONCLUSIONS

In this article, we have studied the effect of various parameters on the estimation of radiation temperature inside indirect-drive ICF hohlraum and also studied the hydrodynamics of foils driven by the hohlraum radiation. A multigroup, one-dimensional, cylindrical geometry, radiation hydrodynamic code is used for this study. Opacities are calculated using a screened hydrogenic average atom model. It is shown that the Rosseland mean opacity of Au-Sm and Au-Gd mixtures are higher than that of any pure material in the mixture for a wide variation of temperatures. This is essentially because of the bound–bound and bound–free contribution to opacities. The low opacity frequency region of one element in the mixture coincides with the high opacity region of the other element. The radiation temperature inside a cylindrical hohlraum is seen to be strongly dependent on the number of frequency groups used. One group radiation transport underpredicts the radiation temperature. It is also seen that erroneous results can be obtained if the space mesh in the hohlraum wall is not fine enough. The spectrum of the radiation is also seen to be different from Planck, especially in the high-energy range. This may lead to preheating of the target.

REFERENCES

ARMSTRONG, B.H. & NICHOLLS, R.W. (1972). *Emission, absorption and transfer of radiation in heated atmosphere.* Oxford: Pergamon Press.

BENNET, B.I., JOHNSON, J.D., KERLEY, G.I. & ROOD, G.T. (1978). *Recent developments in the Sesame equation-of-state library.* Report No. LA-7310. New Mexico: Los Alamos National Laboratory.

COLOMBANT, D., KLAPISCH, M. & SHALOM, A. BAR (1998). *Phys. Rev. Lett.* **57**, 3411–3416.

ERMOLOVICH, V.F., REMIZOV, G.N., ROMANOV, YU.A., RYABIKINA, N.A., SHAGALIEV, R.M., VAKHLAMOVA, L.L., VATULIN, V.V., VINOKUROV, O.A., KANG, K.H., MARUHN, J.A. & BOCK, R. (1998). *Laser Part. Beams* **16**, 525–532.

GUPTA, N.K. (1999). *Comparison of numerical simulations and published experimental results for the radiation hydrodynamics in a wedge shaped aluminium and thin gold foils.* Report No. BARC/1999/E/015. Mumbai: Bhabha Atomic Research Centre.

GUPTA, N.K. & KUMAR, V. (1995). *Laser Part. Beams* **13**, 389–402.

KAUFFMAN, R.L., SUTER, L., DARROW, C.W., KILKENNEY, J.D., KORNBLUM, H.N., MONTGOMERY, D.S., PHILLION, D.W., ROSEN, M.D., THIESSEN, A.R., WALLACE, R.J. & ZE, P. (1994). *Phys. Rev. Lett.* **73**, 2320–2323.

KERLEY, G.I. (1981). *User manual for PANDA: A computer code for calculating equation of state.* Report No. LA-8833-M. New Mexico: Los Alamos National Laboratory.

LINDL, J.D. (1998). *Inertial Confinement Fusion: The quest for ignition and energy gain.* New York: Springer.

MORE, R.M. (1982). *J. Quant. Spectrosc. Radiat. Transfer* **27**, 345–357.

MAYER, H. (1947). *Methods of opacity calculations.* Report No. LA-647. New Mexico: Los Alamos National Laboratory.

NAQVI, A.M. (1964). *J. Quant. Spectrosc. Radiat. Transfer* **4**, 597–615.

NISHIHARA, K., MURAKAMI, M., AZECHI, H., JITSUNO, T., KANABE, T., KATAYAMA, M., MIYANAGA, N., NAKAI, M., NAKATSUKA, M., TSUBAKIMOTO, K. & NAKAI, S. (1994). *Phys. Plasmas* **1**, 1653–1661.

NISHIMURA, H., ENDO, T., SHIRAGA, H., KATO, Y. & NAKAI, S. (1993). *Appl. Phys. Lett.* **62**, 1344–1346.

ORZECHOWSKI, T.J., ROSEN, M.D., KORNBLUM, H., PORTER, J.L., SUTER, L.J., THIESSEN, A.R. & WALLACE, R.J. (1996). *Phys. Rev. Lett.* **77**, 3545–3548.

PERROT, F. (1989). *Phys. Scr.* **39**, 332–337.

RAMIS, R., SCHMALZ, R. & MEYER-TER-VEHN, J. (1988). *Comput. Phys. Comm.* **49**, 475–505.

REMINGTON, B.A., WEBER, S.V., MARINAK, M.M., HANN, S.W., KILKENNEY, J.D., WALLACE, R.J. & DIMONTE, G. (1995). *Phys. Plasmas* **2**, 241–255.

RICHTMYER, R.D. & MORTON, K.W. (1967). *Difference methods for initial value problem.* New York: John Wiley.

RICKERT, A. & MEYER-TER-VEHN, J. (1990). *Laser Part. Beams* **8**, 715–727.

ROSE, S.J. (1992). *J. Phys. B: At. Mol. Opt. Phys.* **25**, 1667–1681.

T-4 GROUP. (1983). *SESAME 83: Report on the Los Alamos equation of state library.* Report No. LALP 83-4. New Mexico: Los Alamos National Laboratory.

WANG, P., MACFARLANE, J.J. & ORZECHOWSKI, T.J. (1997). *Rev. Sci. Instrum.* **68**, 1107–1110.

ZEL'DOVICH, YA.B. & RAIZER, YU.P. (1996). *Physics of shock waves and high temperature hydrodynamics phenomena.* New York: Academic Press.

ZIMMERMAN, G.B. & KRUER, W.L. (1975). *Comments Plasma Phys. Controlled Fusion* **2**, 51.